CrossMark

Analysis of microseismicity associated with the 2017 seismic swarm near the Aegean coast of NW Turkey

Maria Mesimeri[1] · Christos Kourouklas[1] · Eleftheria Papadimitriou[1] · Vassilios Karakostas[1] · Despoina Kementzetzidou[1]

Abstract

A thorough spatiotemporal analysis of the intense seismic activity that took place near the Aegean coast of NW Turkey during January–March 2017 was conducted, aiming to identify its causative relation to the regional seismotectonic properties. In this respect, absolute and relative locations are paired and a catalog consisting of 2485 events was compiled. Relative locations are determined with high accuracy using the double-difference technique and differential times both from phase pick data and from cross-correlation measurements. The spatial distribution of the relocated events revealed a south-dipping causative fault along with secondary and smaller antithetic segments. Spatially, the seismicity started at the westernmost part and migrated with time to the easternmost part of the activated area. Temporally, two distinctive periods are observed, namely an early period lasting 1 month and a second period which includes the largest events in the sequence. The investigation of the interevent time distribution revealed a triggering mechanism, whereas the ETAS parameters show a strong external force ($\mu > 1$), which might be attributed to the existence of the Tuzla geothermal field.

Keywords Earthquake swarms · Relocation · Interevent times · ETAS · Statistical seismology

Introduction

Earthquake swarms are sequences of earthquakes that often start and cease gradually without a distinctive large event (Scholz 2002). Several mechanisms have been proposed to explain the generation of earthquake swarms. A commonly acceptable mechanism relates the earthquake occurrence to an increase in pore pressure caused by fluid flow. As a result, earthquake swarms occur in a region where there is an unusual strong strength gradient; thus, any event in the sequence is prevented from growing very large; strain relief is controlled by the fluid flow, and no dominant large event can occur. For the same reason, the b-value in the earthquake size distribution is often observed to be unusually large in swarms, indicating the absence of large events (Scholz 1968; Sykes 1970; Urbancic et al. 1992; Schorlemmer et al. 2005; Farrell et al. 2009). An interpretation regarding the occurrence of earthquake was first given by Mogi (1963), who considers earthquake swarm activity as an indication of increasing lithospheric heterogeneity. The swarms appearance was considered as an intermediate-term precursor, on the basis of their tendency to occur in and around the focal region several years before the strong mainshock (Evison 1977). Swarms were considered as part of an overall increase in seismicity, the onset of which marks the onset of seismogenesis, and formed the basis for long-term synoptic forecast of strong mainshock along with the Hellenic subduction zone by Evison and Rhoades (2000) alike in New Zealand and Japan.

✉ Maria Mesimeri
  mmesimer@geo.auth.gr

  Christos Kourouklas
  ckouroukl@geo.auth.gr

  Eleftheria Papadimitriou
  ritsa@geo.auth.gr

  Vassilios Karakostas
  vkarak@geo.auth.gr

  Despoina Kementzetzidou
  dkementz@auth.gr

[1] Geophysics Department, School of Geology, Aristotle University of Thessaloniki, 54124 Thessaloniki, Greece

Earthquake swarms were not thoroughly studied in Greece during the past decades, mainly because of the sparsity of the seismological network and the poor azimuthal coverage. However, in the last decade their identification and study were increased mainly due to the improvement of the geometry of the Hellenic Unified Seismological Network (HUSN). The deployment of local seismological networks operated for a short time in several areas further contributed to their investigation. The April 2007 Lake Trichonis swarm with three events of magnitudes between 5.0 and 5.2 provided an abundance of data for revealing regional seismotectonic properties (Kiratzi et al. 2008). In addition to the seismological recordings, the slip calculated by geodetic measurements was used for investigating the spatial evolution of a swarm that lasted for about six (6) months in 2011, with three events of $M_w \geq 4.6$ that occurred near the city of Kalamata (southern Greece) by Kyriakopoulos et al. (2013). The aforementioned cases are related to the back arc deformational environment, whereas a remarkable case concerns the 2006 earthquake swarm, which comprised eleven (11) earthquakes with magnitudes ranging in 4.9–5.6, taking place in Zakynthos Island, at the northwestern part of the Hellenic subduction zone (Papadimitriou et al. 2013).

Considerable work was conducted in the area of Corinth Gulf where the appearance of earthquake swarms is a common characteristic of seismic activity (e.g., Pacchiani and Lyon-Caen 2010; Karakostas et al. 2012; Mesimeri et al. 2013; Duverger et al. 2015). The intensification and elongated duration in some cases in particular attracted the attention and interest of multiple research groups, like the case of the 2013 Aigion swarm (Chouliaras et al. 2015; Kapetanidis et al. 2015; Mesimeri et al. 2016). The installation of local networks substantially improves the quality and abundance of the recordings, like in the case of the vigorous swarm in the area of Florina, NW Greece, that took place during July 2013–January 2014 and evidenced the fluid-driven seismogenesis (Mesimeri et al. 2017).

The occurrence of swarms associated with strike-slip faulting is identified in the area of Aegean Sea. An earthquake swarm near Psara Island, in the central Aegean Sea, was studied using data from a local digital seismological network operated during April–June 2002 (Karakostas et al. 2010). This supported the existence and activation of the conjugate sinistral strike-slip faults in the area after they firstly attested with the 2001 Skyros earthquake (Karakostas et al. 2003). An earthquake occurred on 2013 January 8 M_w5.8 in North Aegean, to the northwest of our study area, on a fault segment in the continuation of the 1968 $M = 7.5$ rupture. It was followed by a handful of $M \geq 4.0$ aftershocks and tens of $M \geq 3.0$. The specific fault segment was not associated with a known strong historical earthquake and this intrigued the investigation of

its frictional properties, by testing the agreement of off fault seismicity with stress enhanced areas, thus evidencing high fault friction (Karakostas et al. 2014).

The microseismicity that took place in the NW coast of Turkey north of Lesvos Island during January 01–March 31, 2017, is analyzed in this study by applying the most effective techniques for earthquake relocation (waveform cross-correlation, double-difference technique) along with a detailed study of the spatiotemporal evolution of the activity. Spatial, temporal and magnitude distributions were analyzed aiming to shed light to the seismicity behavior and reveal properties of the causative faults. The activity is located in an area where major active faults associated with $M \geq 6.0$ are not known, according to the available historical and instrumental data. The earthquake swarm is most probably connected with minor faults accommodating moderate earthquakes ($M \sim 5.0$) as the ones comprised in the current seismic excitation. The temporal occurrence of events, using stochastic models (i.e., ETAS), and the interevent times probability density function were examined in order to associate their occurrence with a possible fluid source.

Tectonic setting and regional seismicity

The activated area (box in Fig. 1) is located near the northeastern Aegean coastline of western Turkey, an area constituting part of the back arc Aegean region (Fig. 1). The subduction of the oceanic lithosphere of the Eastern Mediterranean under the Aegean microplate, along with the Hellenic Arc, and the prolongation of the North Anatolian Fault (NAF), along with the North Aegean Trough (NAT) into the Aegean (Fig. 1), are the driving mechanisms of the active deformation in this area. The dextral strike-slip NAF constitutes an active boundary along with the Anatolian microplate and is moving fast to the west at a rate of ~ 24 mm/year. This motion is translated into the Aegean Sea where an additional N–S extension of ~ 11 mm/year is added due to the slab rollback, integrated to the SW motion of ~ 35 mm/year of the south Aegean relative to Europe.

The study area (box in Fig. 2) is characterized by sparse low in magnitude instrumental seismicity, whereas it is surrounded by strong ($M \geq 6.0$) historical earthquakes (yellow stars in Fig. 2), both offshore and onshore. This implies that the deformation is not controlled by a dominant major fault, but it rather comprises smaller fault segments. The most recent strong earthquake ($M = 6.9$) occurred in 1944 on Ayvacik fault segment (Fig. 2, gray line) and the second last in 1865 ($M = 6.6$) in the adjacent Edremit fault segment (Fig. 2, black line), both bounding the southern coastline of the study area. The westernmost
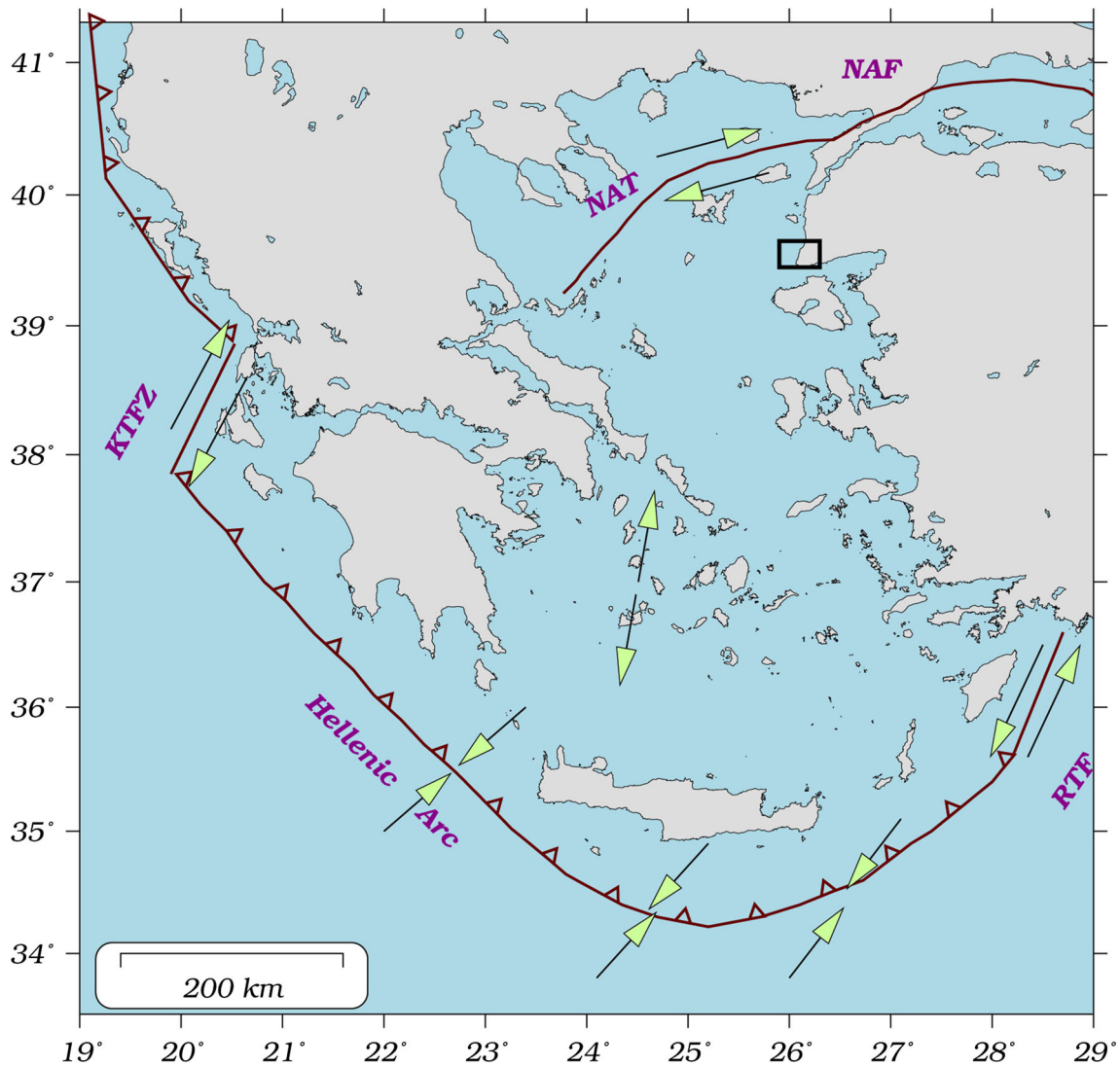
Fig. 1 Major active boundaries and relative motions in the broader Aegean region. *KTFZ* Kephalonia Transform Fault Zone, *NAT* North Aegean Trough, *NAF* North Anatolian Fault, *RTF* Rhodos Transform Fault. The study area is depicted by a rectangular

segments of this branch were successively failed in 1981 in a doublet just a week apart, with the first mainshock of $M = 6.8$ on December 14 and the second one of $M = 6.5$ on December 27. The lack of strong ($M \geq 6.0$) historical and moderate ($M \geq 5.0$) instrumental earthquakes in the currently activated area advocates the thorough investigation of the 2017 swarm, aiming to disclose the deformational pattern that constitutes indispensable component for the seismic hazard assessment in both local and regional scales.

Data

A catalog of 2485 earthquakes (Fig. 3) covering 3 months of seismic activity (January 1–March 31, 2017) was initially compiled based on the bulletins of three different Institutes, namely the Geophysics Department of Aristotle University of Thessaloniki (GD-AUTh, http://geophysics.geo.auth.gr/ss/station_index.html), the Geodynamic Institute of Athens (NOA, www.gein.noa.gr) and the Kandili Observatory and Earthquake Research Institute (KOERI, www.koeri.boun.edu.tr/sismo/2/en/). All the available P and S phases marked at 25 seismological stations with epicentral distances less than 200 km (Fig. 3) were gathered and merged for common events. Additionally, the daily recordings of the stations that belong to the HUSN and the KOERI were archived.
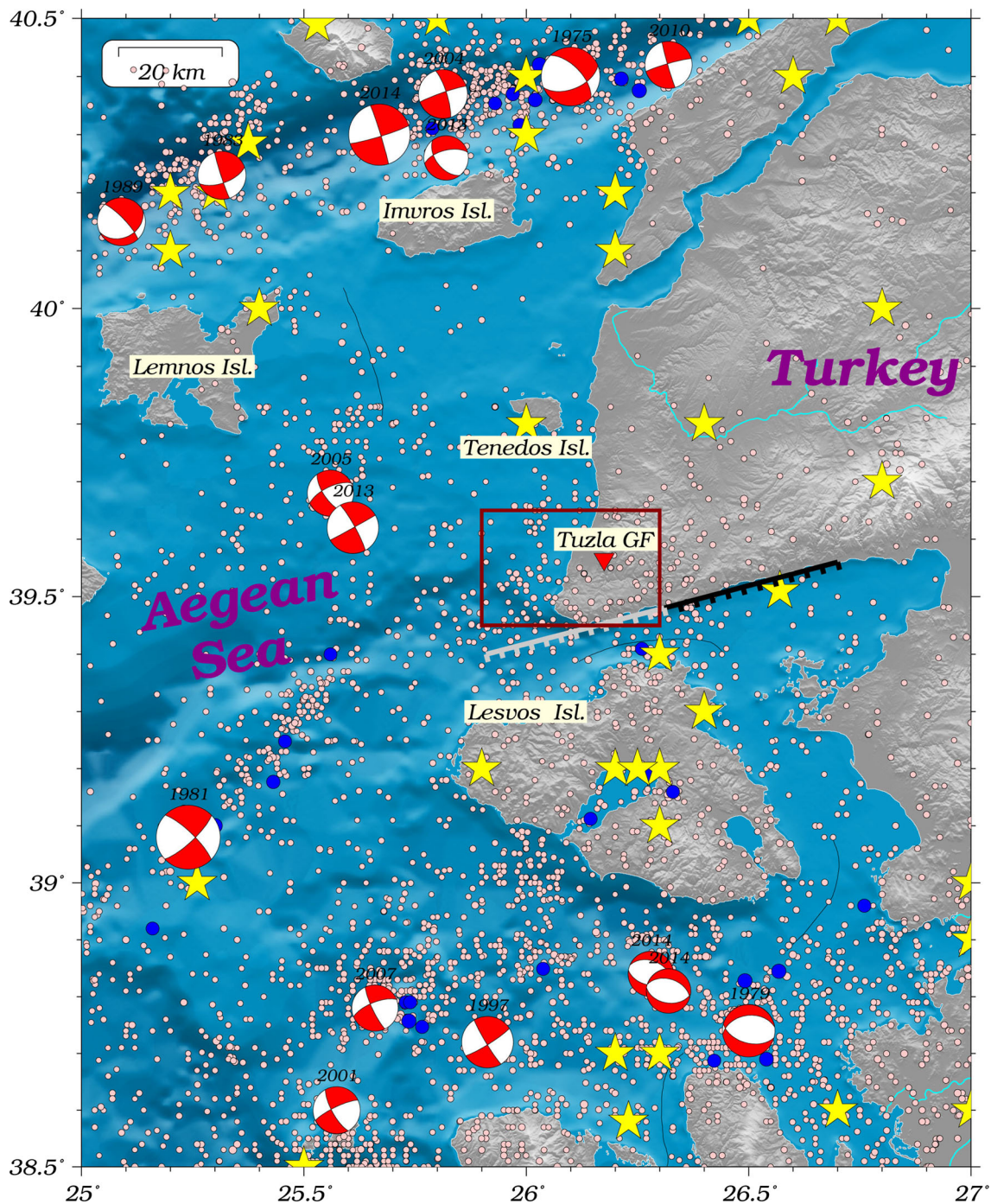
Fig. 2 Regional seismicity is shown along with known fault plane solutions for the stronger ($M \geq 5.2$) events that occurred during the last 50 years. The epicenters of the known historical earthquakes with $M \geq 6.0$ are shown as stars. Larger and smaller circles depict earthquakes with $M \geq 5.0$ and $M \geq 3.5$, which occurred since 1912 and 1971, respectively. The Edremit and Ayvacik faults are shown in gray and black lines, respectively

Relocation

A dataset of 819 earthquakes that have been recorded at ten stations at least is selected for the relocation. The earthquake absolute location is achieved using the HYPOIN-VERSE software (Klein 2000) along with an estimated, using Wadati's method, Vp/Vs ratio equal to 1.75 and a regional velocity model (Table 1) (Panagiotopoulos and Papazachos 1985). Stations delays are calculated in order to improve the performance of the 1D velocity model, which does not account for lateral crustal variations. The obtained solutions were used as input to the relative
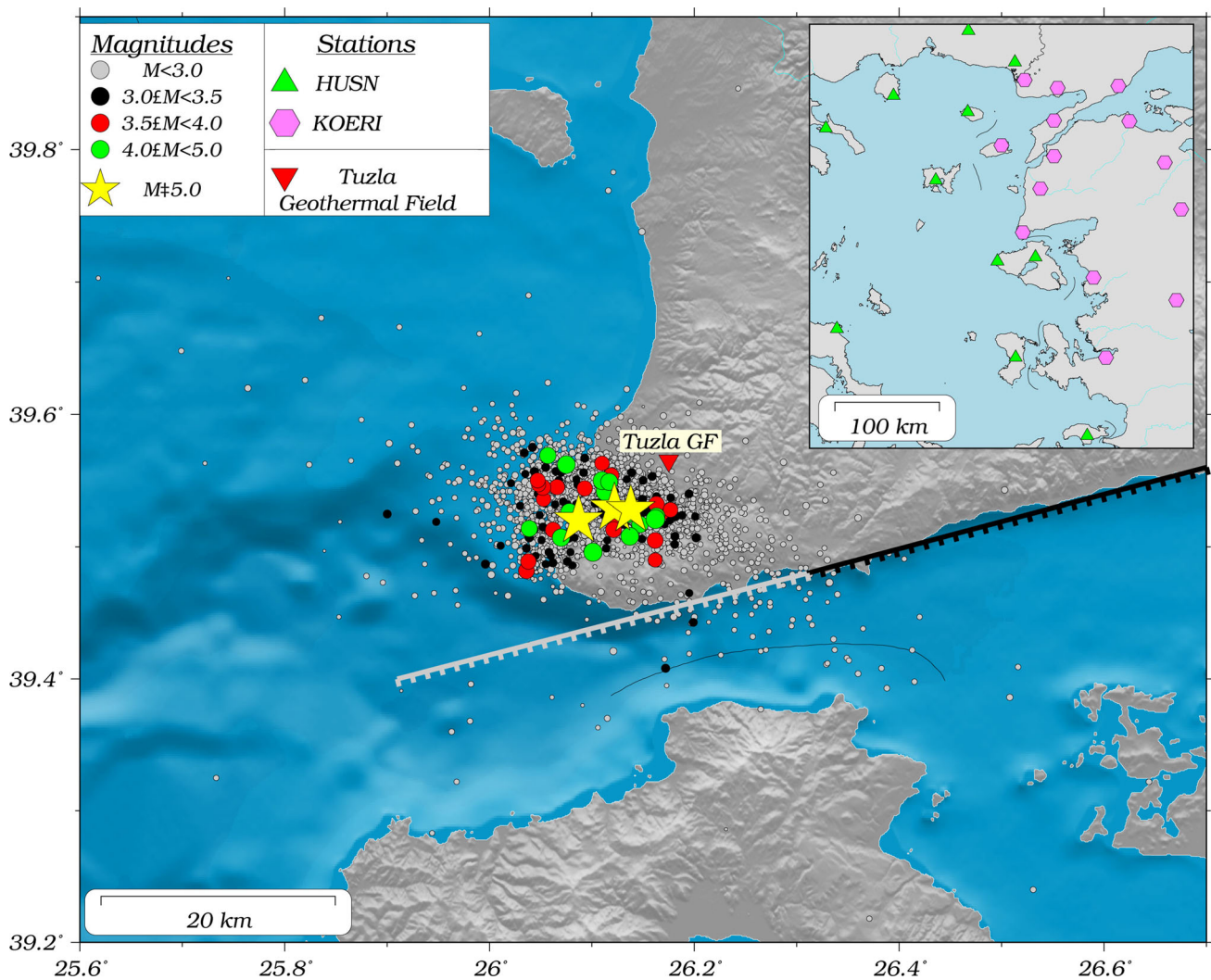
Fig. 3 Epicentral distribution of the initial locations of the events occurring from January 1 to March 31, 2017. The Edremit and Ayvacik faults are shown in gray and black lines, respectively. Inset map: Spatial distribution of the seismological stations, the recordings of which were used in this study. Stations from HUSN are shown in green triangles and stations from KOERI with magenta hexagons

Table 1 Velocity model used in this study from Panagiotopoulos and Papazachos ([1985](#))

Depth (km)	Velocity (km/s)
0.0	6.0
19.0	6.6
31.0	7.9

relocation procedure that was performed using the double-difference method (Waldhauser and Ellsworth [2000](#)). At this step, the phase picked data were combined along with cross-correlation differential times. The daily recordings were modified accordingly in order to get waveforms bandpass filtered at a range of 1.5–10 Hz with 60-s duration and updated for the P and S picks. Then, cross-correlation was performed in the time domain (Schaff and Waldhauser [2005](#)) using a 2-s window around P and S picks,

respectively. The event pairs with correlation coefficient (CC) greater than 0.7 and with at least 4 P or 4 S differential times were considered for the relocation. The final relocated catalog, which was produced after appropriate re-weighting of the inversion scheme, contains 724 events. The median location errors were estimated using a bootstrapping method and are 762, 338 and 641 m for the X, Y and Z direction, respectively.

The events that were not included in the previous dataset were relocated using only the HYPOINVERSE software, along with the aforementioned Vp/Vs ratio and crustal model. The absolute locations were merged with the relative ones for compiling a catalog containing all the events. The highly accurate earthquake catalog, with the relative locations, is used for the investigation of spatial properties of the seismic activity (see section "Spatial evolution of

seismic activity"), whereas the one containing all the available solutions, namely both relative and absolute locations, was used for studying the temporal evolution of the activity (see section "Temporal evolution of the seismic activity").

Spatial evolution of seismic activity

The relocated catalog was used for investigating, the spatial evolution seeking to reveal the cascading activation pattern of the causative fault segments. The epicentral distribution reveals a seismic zone of 17 km length (Fig. 4a). The events are located both onshore and offshore and can be distinguished into two clusters, spatially related and probably associated with different fault segments. The first cluster is aligned at an approximately 295° direction and contains the vast majority of the relocated events along with the three stronger ones with $M \geq 5.0$ (stars in Fig. 4a). The southern cluster with a total length of less than 5 km comprises lower in magnitude events (all with $M < 4.0$). The distinction of the two clusters is also evidenced in the strike–normal cross section (Fig. 4b). Particularly, the focal distribution of the northern cluster reveals a south-dipping structure at an angle of about 45°, whereas the southern one can be associated with a north-dipping segment with an angle of $\sim 60°$.

In an attempt to unfold the spatial evolution of the seismicity, different snapshots, based on the temporal

evolution of the activity (see section "Temporal evolution of the seismic activity"), are shown in map view (Fig. 5), in strike–normal (Fig. 6) and along-strike (Fig. 7) cross sections. Figure 5a illustrates the spatial extension of the $M \geq 3.0$ earthquakes that occurred during January 01–March 31, 2017. The earthquakes are drawn by different colors indicating the different temporal window, along with the fault plane solutions for several of them, depicted as lower-hemisphere equal-area projections. This epicentral distribution covers an area ~ 14 km long, capable of accommodating an $M \sim 6.0$ earthquake. The lack of relevant information, however, and the cascade-type failure of adjacent smaller fault segments advocate for a swarm type activation of this area. Figure 6a shows the focal distribution of the $M \geq 3.0$ events along with the fault plane solutions, keeping the same notation as in Fig. 5, whereas Fig. 7a illustrates the spatial evolution of the activity. This evidences the existence of the two conjugate faults, as shown and discussed in Fig. 4.

In the first 35 days, the $M \geq 3.0$ seismic activity mainly followed a stripe both offshore and onshore (Fig. 5b), implying, along with the available fault plane solutions, an ENE–WSW strike of the causative faults. The lower in magnitude seismicity (depicted with white circles Fig. 5b) is spread in a much broader area; however, it also forms a seismic zone with the same trend. The two stronger events ($M = 4.4$ and $M = 4.0$) occurred on the 14th and 15th of January, respectively, very close in time (about 5 h interevent time) and space. The south-dipping structure is
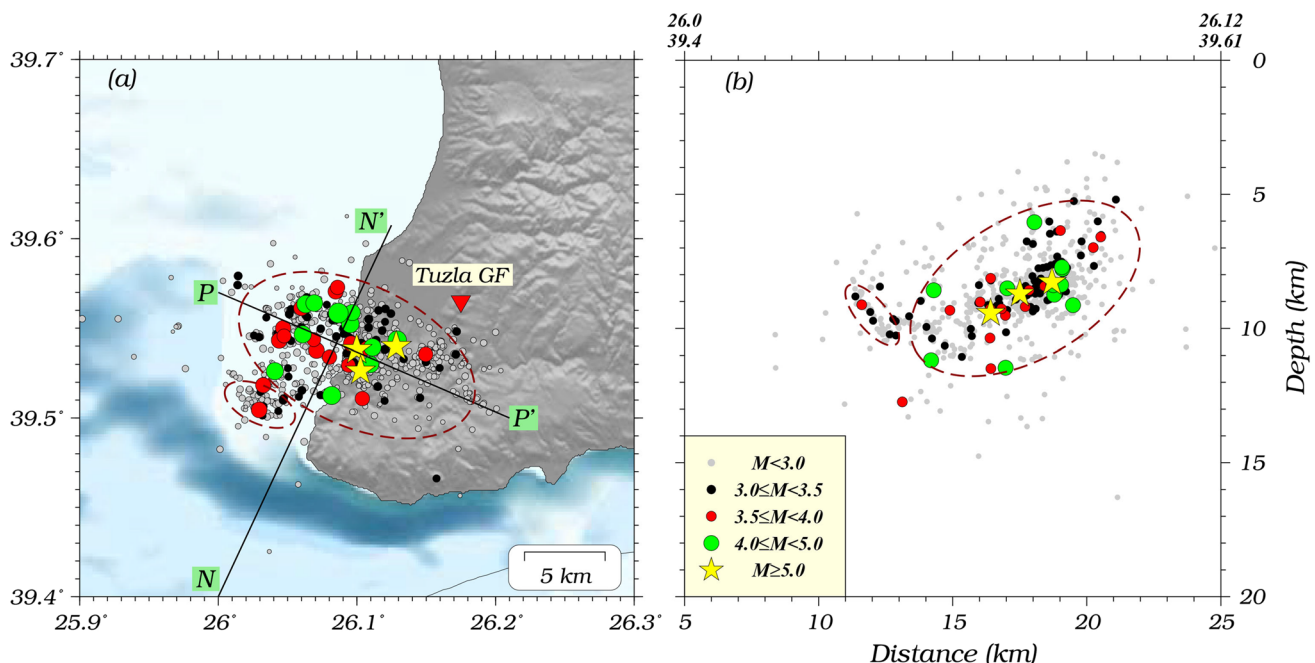


Fig. 4 a Epicentral distribution of the relocated events and b cross section along the line N–N′ normal to the dominant strike with 20 km width. Dashed lines enclose the events that are located on different fault segments
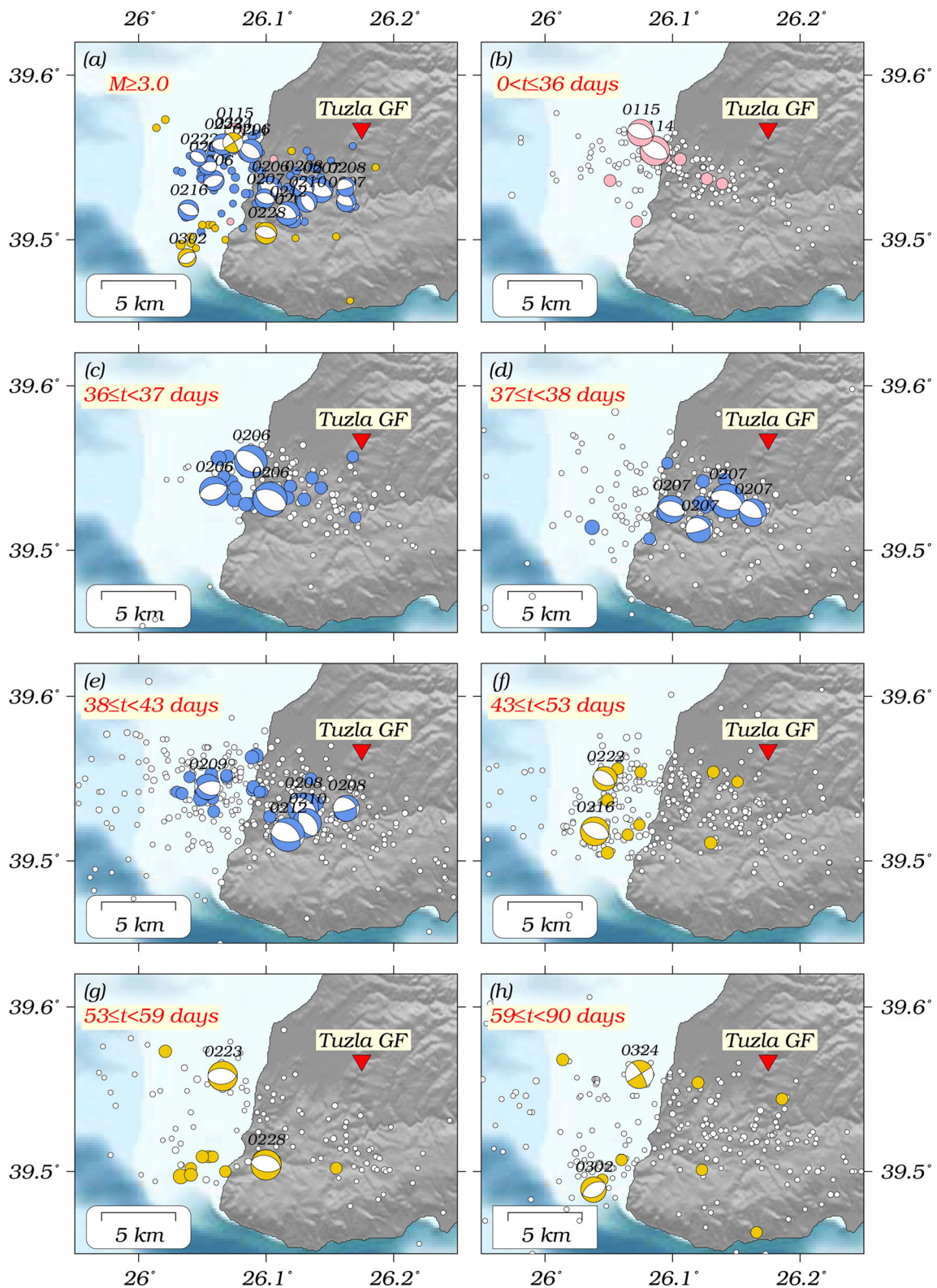
Fig. 5 Spatial distribution of seismicity along with the available fault plane solutions for the events occurred during **a** 0–90, **b** 0–36, **c** 36–37, **d** 37–38, **e** 38–42, **f** 43–53, **g** 54–31, **h** 62–90 days

Fig. 6 Cross sections in different time intervals (same as Fig. 5) corresponding to N–N′ line of Fig. 5
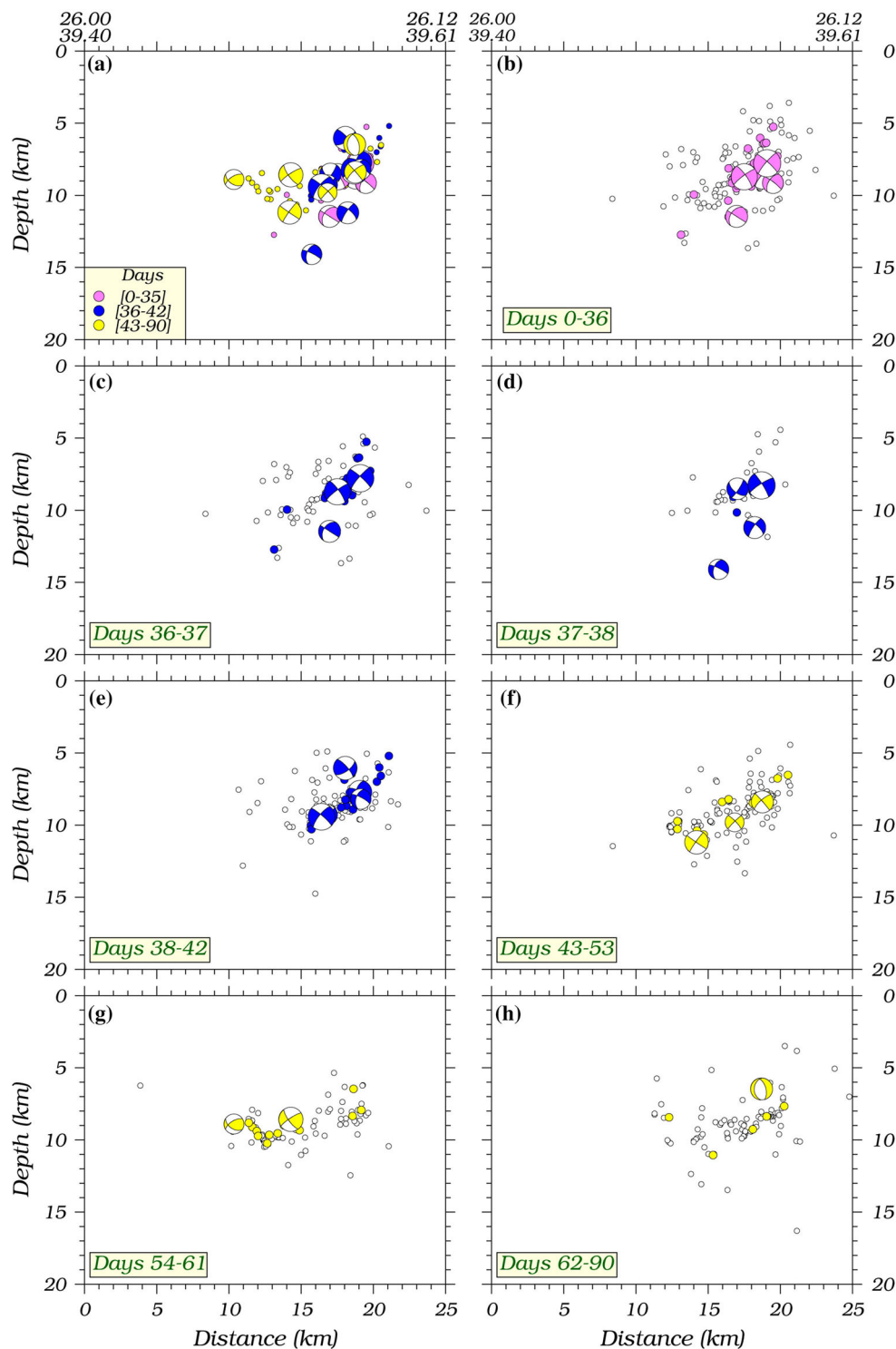

well defined by their focal distribution in the strike–normal cross section (Fig. 6b) which is in accordance with the one of the nodal planes of the available fault plane solutions. Figure 7b shows that the activity started on the westernmost part of the area.

The activity attenuated with time and then was intensified on the 6th of February, namely 22 days later, with three earthquakes of $M = 4.9$, $M = 5.1$ and $M = 4.3$ on the same day (Fig. 5c). One more striking feature of the activity is the intensification of the $M \geq 3.0$ events that now are migrated to the east and occupy almost the entire

Fig. 7 Strike parallel (P–P′ in Fig. 4) cross sections of seismicity in different time intervals (same as Fig. 5)
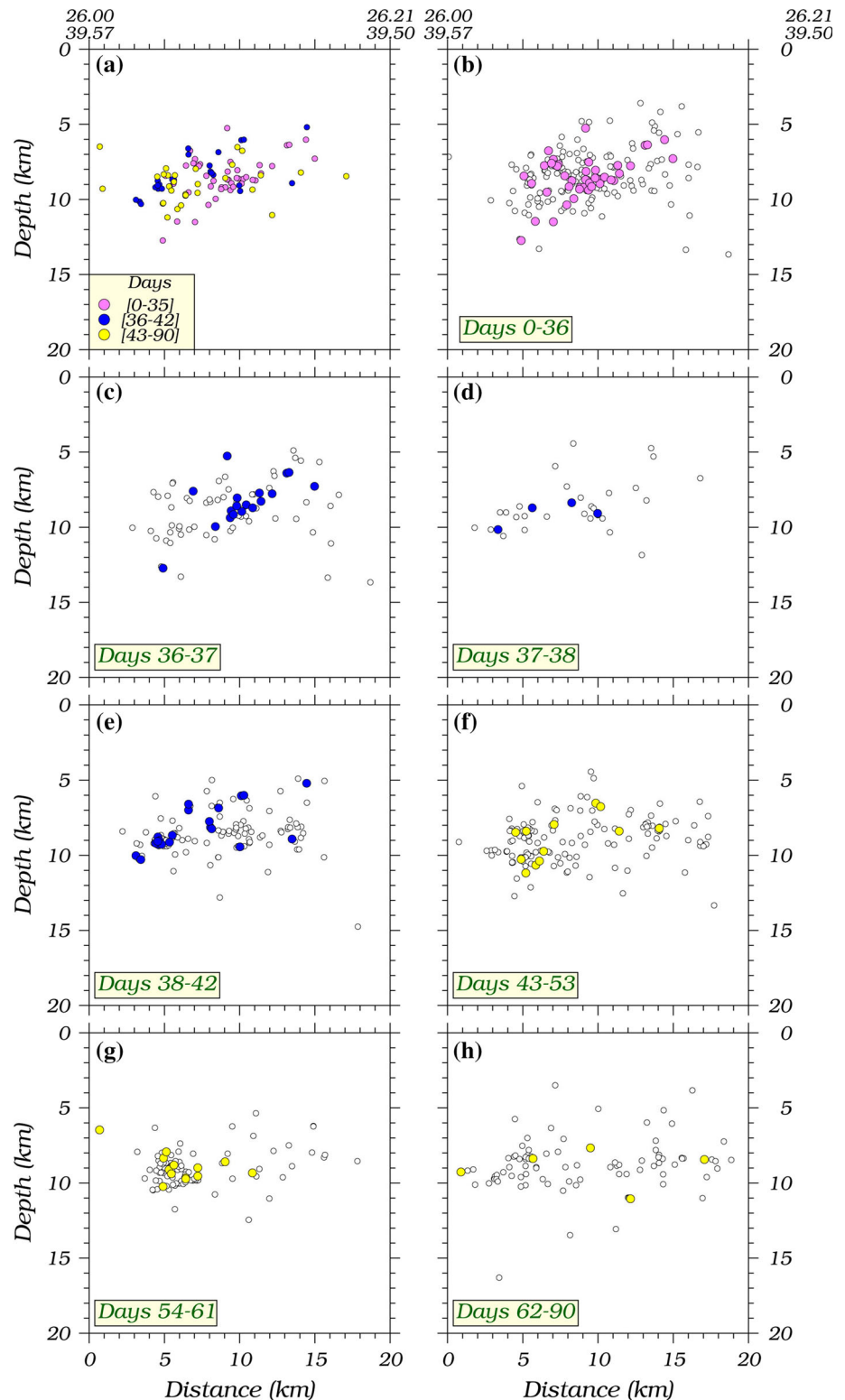
activated area (blue circles in Figs. 5c, 7c). On the next day, 7th of February, the strong events (M = 5.1, 4.1, 4.1 and 4.0 shown as beach balls at their epicentral locations) are now located at the eastern part (Figs. 5d, 7c). The seismic activity remained high and gradually attenuated in

the next 5 days with the stronger events (M = 4.6, 3.9, 4.3 and 5.0) located at the eastern part. On February 9, a M = 3.8 occurred at the western offshore part, along with several M ≥ 3.0 located at the same area (Figs. 5e, 7e). During this period, the events are comprised in a south-

dipping seismic zone which is repeatedly activated (Fig. 6c–e).

Later, on the 43rd day (February 16) a gradual increase in seismic activity appeared along with a westward migration to the western offshore area. Most of the events are concentrated around the stronger earthquakes of $M = 4.3$, $M = 3.6$ and $M = 4.4$, occurred between the 46th and 53rd day of activity and are shown as beach balls (Figs. 5f, 7f). This provides evidence for an offshore fault network composed of small fault segments since the activity continues there. The next cluster of the stronger events ($M = 4.5$ and $M = 3.8$ along with the $M \geq 3.0$ ones) occupies now the southwestern part (Figs. 5g, 7g). The activity decreases with time, and a limited number of $M \geq 3.0$ earthquakes are observed in between the 62nd and 90th days. In that time, only one distinctive event of $M = 4.2$ on 24th of March, exhibiting a different faulting type (Figs. 5h, 7h), occurred. The complexity of the fault network geometry is depicted in the last three cross sections (Fig. 6f–h). Initially, the south-dipping fault seems to be activated (Fig. 6f), whereas few days later on the 53rd day the activity is concentrated onto an antithetic north-dipping small fault segment (Fig. 6g). Finally, the last cross section shows that the seismicity again occupies the area where the south-dipping segment is located (Fig. 6h).

The focal mechanisms plotted in Fig. 5 show a rather limited diversity of faulting type, competing between normal faulting and strike slip, with most of them exhibiting an oblique motion. The strike-slip motion that prevails in Northern Aegean influences the deformation style and conveys the oblique component in the back arc N–S extensional stress field.

Temporal evolution of the seismic activity

The temporal properties and evolution of the 3-months' seismic activity were examined by using the catalog of 2485 events, which contains both absolute and relative relocations. Firstly, we calculated the completeness magnitude with the goodness-of-fit method (Wiemer and Wyss 2000) and found it equal to 2.0. The values of the a and b parameters were estimated using the MLE method and found equal to 5.62 and 1.13, respectively. The b-value being larger than unity indicates a swarm-like behavior.

The cumulative number of events along with seismicity rate (events per day) of the complete catalog is shown in Fig. 8. A low seismicity rate is observed for the first 13 days, whereas a gradual increase appeared on day 14 and day 27. On day 35, an abrupt change is observed with several lower magnitude events as well as earthquakes with $M \geq 5.0$. The daily rate exhibits several remarkable fluctuations with periods of elevated activity along with

quiescent ones. The seismicity rate changes are highly related to strong events according to the magnitude distribution (Fig. 8b).

The seismic activity might be distinguished in two different periods based on the seismicity rate, namely from the 1st of January up to the 6th of February, right before the occurrence of the strongest event, and from the 6th of February up to the end of the study period. The first period can be considered as preparatory to the second one where the strongest events ($M \geq 5.0$) occurred and the seismicity rate is increased. Further on, the two periods could be divided into smaller sub-periods based on the variations of the daily occurrence rate along with the occurrence of earthquakes with $M \geq 4.0$. These sub-periods are clearly distinguished in Fig. 8 and are used to determine the temporal properties of the seismic activity. For this purpose, we examine the evolution of seismic activity in each sub-period by applying the epidemic-type aftershock sequence (ETAS) stochastic model (Ogata 1998) and by determining the best-fitting probability density function to the empirical interevent time distribution.

ETAS is a stochastic point process model, which considers that seismic activity in a given area consists of two components, the independent background seismicity rate, μ, and the aftershock occurrence rate. The conditional intensity function, $\lambda(t)$, of ETAS model is the sum of these two components and is given by

$$\lambda(t) = \mu + \sum_{\{i, t_i < t\}} \lambda_{(i)}(t) = \mu + \sum_{\{i, t_i < t\}} \frac{K}{(c + t - t_i)^p} e^{a(M_i - M_c)}$$

(1)

where K, c, p and α (alpha) are constants, M_i is the magnitude of each event occurred at time t_i and M_c is the completeness magnitude. In this study, the five parameters (μ, K, c, p and α) were estimated using the simulated annealing algorithm proposed by Lombardi (2015) implemented in the software package SEDA (Lombardi 2017). The model that best fits was selected by the parameters combination that returns the largest log-likelihood value. Each optimal model was then tested using the residual analysis, which transforms the occurrence time of every event, t_i, into τ_i times by the theoretical cumulative function (Ogata 1992)

$$\tau_i = \int_0^{t_i} \lambda(t) \mathrm{d}t$$

(2)

The transformed time, τ_i, expresses the expected number of events, which are expected to occur in the time interval $[0, t_i]$. When the estimated model describes adequately the temporal evolution of the process, the cumulative number of events versus transformed time plot should be linear
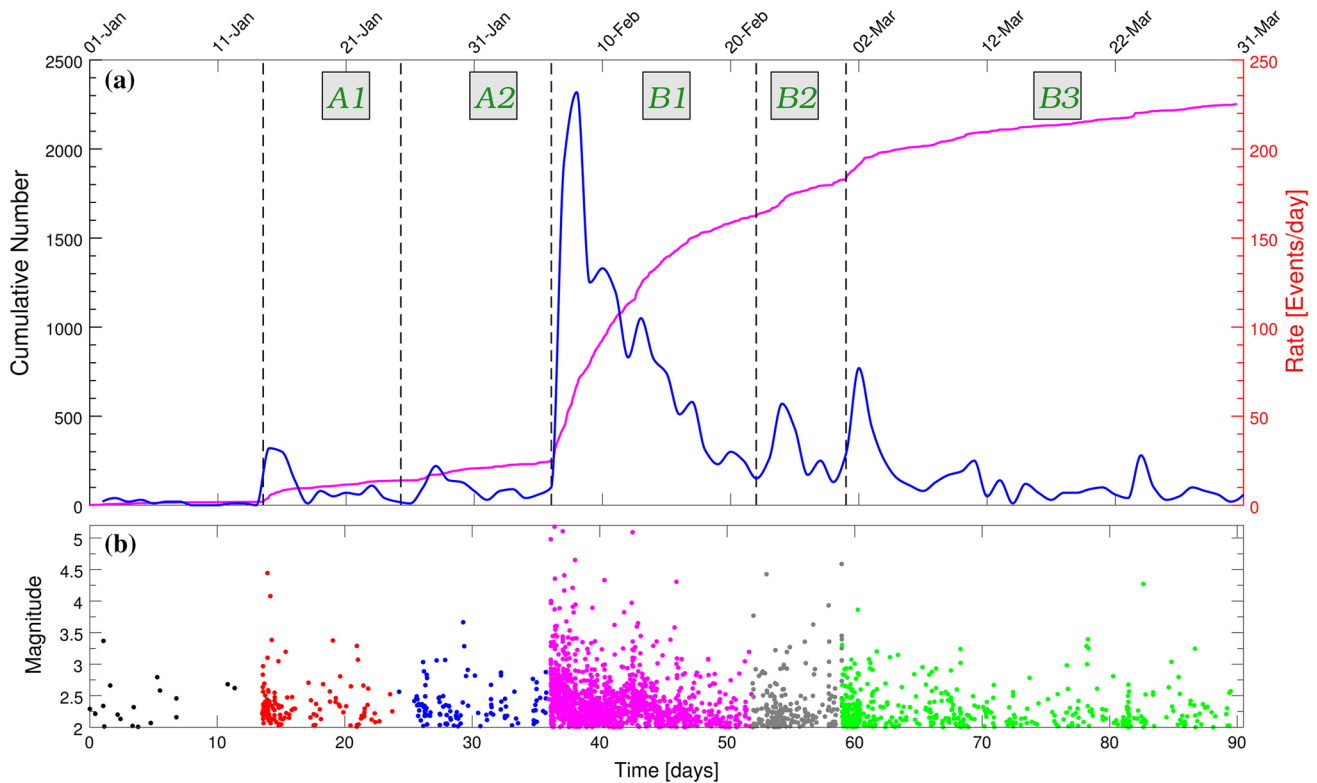
Fig. 8 a Cumulative number of events (left vertical axis; magenta line) along with seismicity rate (right vertical axis; blue line) against time. The distinctive sub-periods (A1, A2, B1, B2, B3) of the sequence are denoted with dashed vertical lines. **b** Magnitude distribution with time for the different sub-periods

with slope equal to unity, indicating a Poison process. Otherwise, the observed number of events presents positive and/or negative deviations from the expected ones. The stability of each optimal model was tested by calculating the branching ratio, n, (Sornette and Werner 2005)

$$n = \frac{K}{(p-1)c^{(p-1)}} \frac{1 - e^{(-\beta-\alpha)(M_{\max}-M_{c})}}{1 - e^{-\beta(M_{\max}-M_{c})}} \qquad (3)$$

where $\beta = b \ln(10)$. According to this formula, a model can be considered stable for values of branching ratio lower than the unity ($n < 1$) (Sornette and Helmstetter 2002).

The ETAS model was applied in each sub-period separately (A1, A2, B1, B2, B3), and the results of the estimation of the parameters are given in Table 2. In all cases, the value of branching ratio was found less than 1, and consequently, the optimal models of each sub-period can be considered as stable. Particularly, in the first part of

period A (A1 in Fig. 9) as well as in the second one (A2 in Fig. 9), the ETAS model does not fit the observed earthquake rate. This is more clearly illustrated when the cumulative number of events is plotted against transformed time (Fig. 9 lower panel). The positive deviations from the model show that the earthquake occurrence is underestimated by ETAS. The estimated parameters present large variations between the two different sub-periods. The μ value, which represents the background rate, is above 1 for both sub-periods, starting from 2.7 in A1 and reaching 5.1 in B2, indicating a possible external force (i.e., fluid intrusion). Parameter α, which defines the ability of an earthquake M_i to trigger another event, has a typical mainshock–aftershock value for sub-period A1 ($\alpha = 1.35$) compared to other studies (e.g., Ogata 1992; Hainzl and Ogata 2005). The α value in A2 equals to 0.517, a value most frequently observed in earthquake swarms. The

Table 2 ETAS estimated parameters (μ, K, p, c, α), the log likelihood, the Akaike information criterion, the branching ratio and the number of observations for each sub-period

Sub-period	μ	K	p	c	α	lnL	AIC	Branching ratio	Obs
A1	2.71	0.03	1.94	0.08	1.35	216.74	− 443.49	0.80	121
A2	5.10	0.07	2.58	0.05	0.51	159.64	− 329.29	0.52	107
B1	5.35	0.05	1.48	0.03	1.08	5202.84	− 10,416.69	0.99	1406
B2	8.95	0.01	2.35	0.06	1.17	486.05	− 982.10	0.82	184
B3	3.52	0.03	1.63	0.03	1.21	816.68	− 1643.43	0.94	417

Fig. 9 (Upper panel) Observed cumulative number of events (black line) along with expected (red line) by ETAS model against ordinary time and transformed time (lower panel) for two sub-periods (A1–A2). The magnitude distribution is shown on the right axis
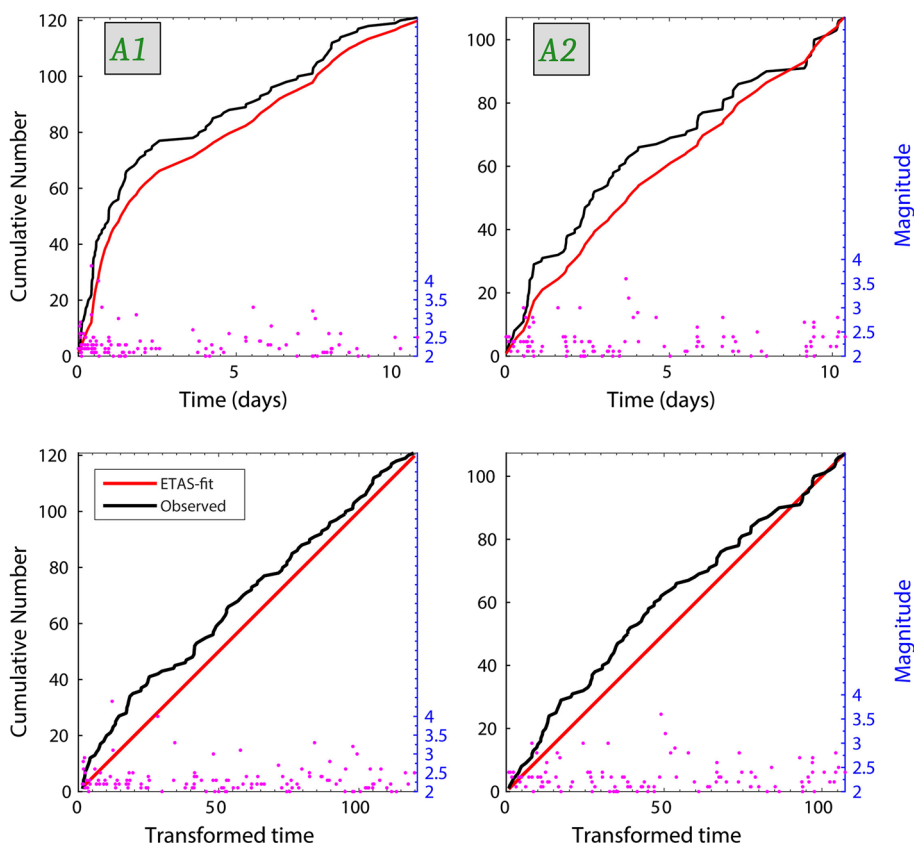

different types of subsequences in period A are also illustrated by the magnitude distribution (Fig. 9 right axis). In A1 sub-period, a strong event with $M = 4.4$ occurred early in the sequence, followed by a $M = 4.0$ event and several lower magnitude earthquakes. In A2 sub-period, all events are almost equivalent in magnitude with the largest one of $M = 3.6$. This verifies the more swarm-like behavior of the second part of period A.

Period B, further divided into three sub-periods (B1, B2, B3), includes the three largest events ($M \geq 5.0$) and is the most active period. Figure 10 depicts the observed cumulative number of events against the predicted by ETAS model in ordinary time and transformed time for each sub-period, respectively. B1 is the best fitted by ETAS model sub-period with very small deviations between the observed (black) and expected (red) seismicity rates. Similarly to period A, the seismicity in sub-periods B2 and B3 is underestimated by the ETAS model mainly due to the abundant low magnitude earthquakes, which are not associated with a large event at the beginning of each sub-period. Regarding the estimated parameters, the value of μ increases in B1 ($\mu = 5.3$) and B2 ($\mu = 8.9$) and decreases in sub-period B3 ($\mu = 3.5$). Parameter α has a value near unity in the three sub-periods, implying a rather mainshock–aftershock behavior.

The deviations between the observed and predicted seismicity rate in transformed time evidence the possibility that the interevent times in each sub-period are not drawn from a Poisson distribution. In this respect, we attempt to calculate the empirical probability density function of the interevent times and compare it to known statistical distributions (i.e., lognormal, Weibull, gamma and exponential) in order to find the best-fitting one. The interevent times are defined as in Corral (2006), and the parameters for each distribution are estimated by applying the MLE method. The comparison of the distributions is performed by the nonparametric Kolmogorov–Smirnov test (K–S test), which is implemented by measuring the absolute distance between cumulative density functions of the examined distributions and the empirical one. The values of Akaike and Bayesian information criteria (AIC and BIC) are calculated as an additional comparison criterion.

The estimated parameters for each distribution, the values of log-likelihood functions along with the K–S test and the information criteria are presented in Table 3. The fitted distributions for the periods A and B are shown in Figs. 11 and 12, respectively, along with the empirical interevent time distribution. In all cases, the lognormal distribution better describes the interevent time distribution with the lowest values of AIC, BIC and of the K–S test. The least-fitted one is the exponential distribution without been rejected by the K–S
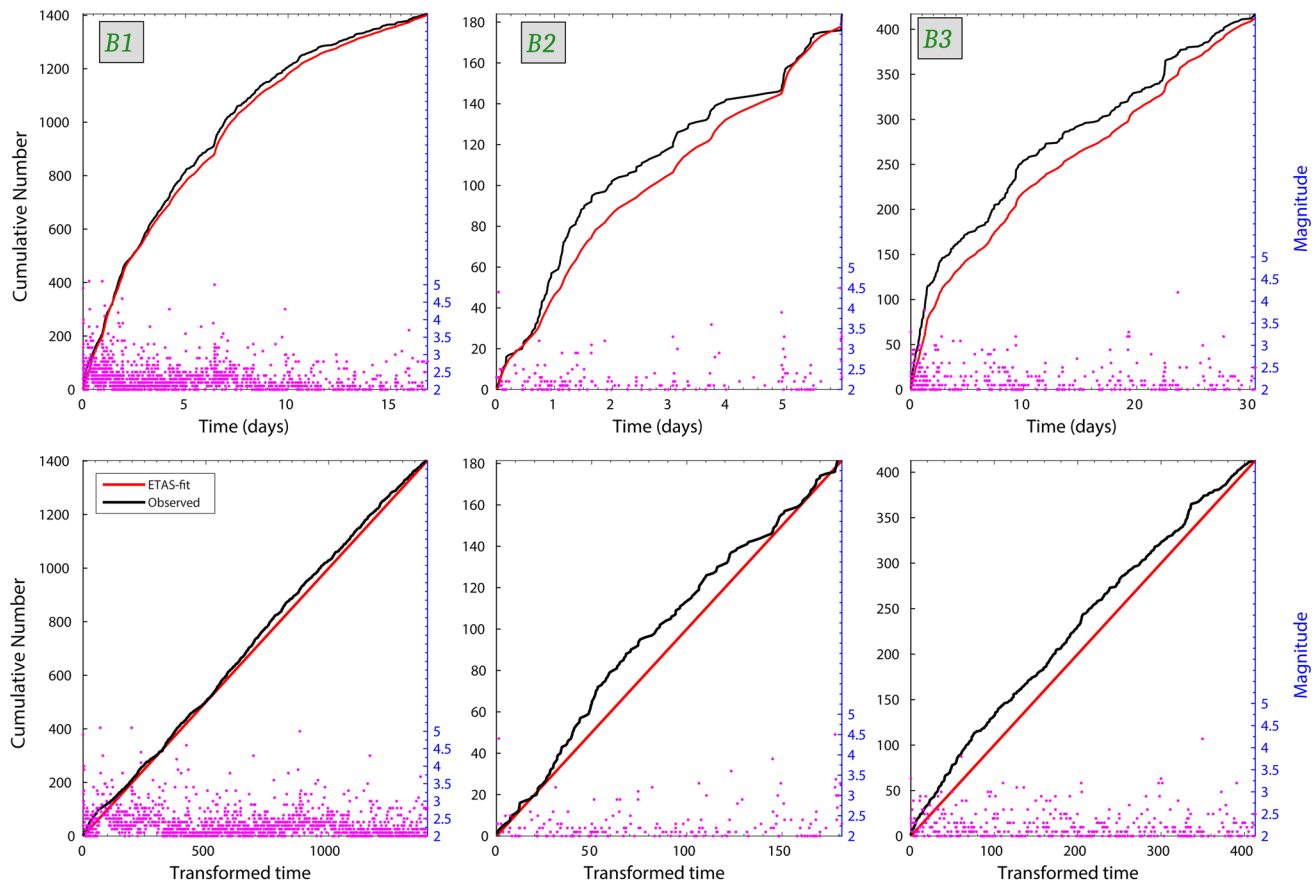
Fig. 10 Same as Fig. 9 for three sub-periods (B1, B2 and B3)

test. Weibull and gamma distributions, on the other hand, are very close to the empirical one. A triggering mechanism is well explained by the fact that lognormal exhibits the best performance in all sub-periods. Particularly, lognormal distribution describes both the short interevent times between subsequent events, which indicate the triggering mechanism, along with late earthquakes in a sequence tangled on the tail of the distribution.

It is worth to notice that the estimated parameters of the lognormal distribution in each sub-period are distinctive. Particularly, it is observed that for period A the two estimated parameters are very similar. On the contrary, in period B1 the two parameters have lower values, as a result of the increased seismic activity meaning that the interevent times are shorter. During the following two sub-periods (B2 and B3), the parameter values increase and are of the same magnitude order with the ones in the early period.

Discussion and conclusions

The 3-month seismic crisis near the Aegean coasts of NW Turkey examined in detail in this study revealed important features regarding the seismogenesis in the area. The

spatial evolution of the activity, investigated using the highly accurate relative locations, revealed that the major activated fault segments are oblique south-dipping normal faults, well suited with the regional seismotectonics. These segments were activated in a cascade type during the seismic crisis, along with smaller north-dipping antithetic fault segments. Seismicity migration to the east evidenced that activity might be triggered by fluid pressure changes in the upper crust. This process has been met in many cases in the literature, where the source of fluids is natural or anthropogenic (e.g., Shelly et al. 2013; Fischer et al. 2014; Shapiro 2015; Mesimeri et al. 2017). The possible fluid source here could be related to the active geothermal area of Tuzla located 5 km from the activated area (Demir et al. 2014).

Considering the possibility of fluid-driven activity, an attempt was made to fit the ETAS stochastic model in the observed data and examine the variations of the estimated parameters. In cases of fluid-induced seismicity, the background rate μ refers to the activity forced by pore pressure changes (Hainzl and Ogata 2005). Thus, values of $\mu \gg 1$ indicate an external force, which in most times could be a plausible fluid source. The temporal evolution of the seismic crisis revealed two distinctive periods, period

Table 3 Estimated parameters, 95% confidence intervals for each sub-period and for each distribution along with their values log-likelihood function and the results of KS test, AIC and BIC criteria.

The critical values of KS test for sub-periods A1, A2, B1, B2 and B3 are 0.2716, 0.2772, 0.2663, 0.2772 and 0.2522, respectively

Sub-period	Distribution	Parameters	Conf. interval	logL	KS test		AIC	BIC
					Statistic	p value		
A1	Lognormal	$\mu = -3.53$	[−3.83, −3.23]	194.39	0.06	0.99	−384.78	−382.35
		$\sigma = 1.65$	[1.46, 1.89]					
	Weibull	$\alpha = 0.06$	[0.04, 0.08]	191.46	0.08	0.99	−378.93	−376.49
		$b = 0.66$	[0.58, 0.76]					
	Gamma	$\alpha = 0.55$	[0.44, 0.68]	187.03	0.11	0.82	−370.06	−367.62
		$b = 0.16$	[0.11, 0.22]					
	Exponential	$\mu = 0.08$	[0.07, 0.10]	169.05	0.23	0.11	−336.10	−334.88
A2	Lognormal	$\mu = -3.35$	[−3.66, −3.03]	154.08	0.08	0.98	−304.16	−301.80
		$\sigma = 1.64$	[1.44, 1.898]					
	Weibull	$\alpha = 0.07$	[0.05, 0.10]	154.07	0.09	0.96	−304.14	−301.78
		$b = 0.69$	[0.60, 0.80]					
	Gamma	$\alpha = 0.59$	[0.47, 0.73]	151.62	0.12	0.80	−299.24	−296.89
		$b = 0.16$	[0.12, 0.23]					
	Exponential	$\mu = 0.10$	[0.08, 0.12]	139.32	0.24	0.10	−276.65	−275.47
B1	Lognormal	$\mu = -5.19$	[−5.25, −5.13]	5043.59	0.06	0.99	−10,083.19	−10,080.68
		$\sigma = 1.20$	[1.15, 1.24]					
	Weibull	$\alpha = 0.01$	[0.009, 0.010]	4891.91	0.10	0.90	−9779.98	−9777.32
		$b = 0.80$	[0.77, 0.83]					
	Gamma	$\alpha = 0.77$	[0.72, 0.82]	4846.74	0.14	0.63	−9689.48	−9686.97
		$b = 0.01$	[0.01, 0.01]					
	Exponential	$\mu = 0.01$	[0.01, 0.01]	4814.44	0.18	0.29	−96,268.90	−9625.63
B2	Lognormal	$\mu = -4.31$	[−4.52, −4.10]	465.24	0.06	0.99	−926.49	−924.13
		$\sigma = 1.42$	[1.29, 1.58]					
	Weibull	$\alpha = 0.02$	[0.02, 0.03]	459.62	0.09	0.96	−915.24	−912.89
		$b = 0.76$	[0.68, 0.85]					
	Gamma	$\alpha = 0.69$	[0.58, 0.82]	455.62	0.12	0.82	−907.25	−904.89
		$b = 0.04$	[0.03, 0.05]					
	Exponential	$\mu = 0.03$	[0.02, 0.03]	446.14	0.20	0.24	−890.29	−889.12
B3	Lognormal	$\mu = -3.75$	[−3.92, −3.59]	755.73	0.06	0.99	−1507.47	−1504.73
		$\sigma = 1.68$	[1.58, 1.81]					
	Weibull	$\alpha = 0.05$	[0.04, 0.06]	752.29	0.07	0.99	−1500.58	−1497.84
		$b = 0.66$	[0.62, 0.71]					
	Gamma	$\alpha = 0.55$	[0.49, 0.62]	740.44	0.11	0.81	−1476.89	−1474.16
		$b = 0.12$	[0.10, 0.15]					
	Exponential	$\mu = 0.07$	[0.06, 0.07]	678.76	0.23	0.06	−1355.52	−1354.16

(A) and a period that the strongest events occurred (B). The parameter μ got high values in period A, starting at 2.7 and reaching 5. During the intense activity, and especially in the sub-period B2, μ takes its highest value ($\mu = 9$) indicating a strong external force associated with the nearby Tuzla geothermal field. Later on, it decreases in the last sub-period (B3) but still well above unity ($\mu = 3.5$).

The variations of α parameter can also reveal whether a sequence exhibits a swarm-like behavior [0.35, 0.85] or is of the mainshock–aftershock type [1.2, 3.1] (Ogata 1992; Hainzl and Ogata 2005). During period A, parameter α had values that showed a typical mainshock–aftershock activity at the beginning transformed later into a swarm-like activity at sub-period A2. In B1 and B2 sub-periods, α parameter has a value between the upper and lower
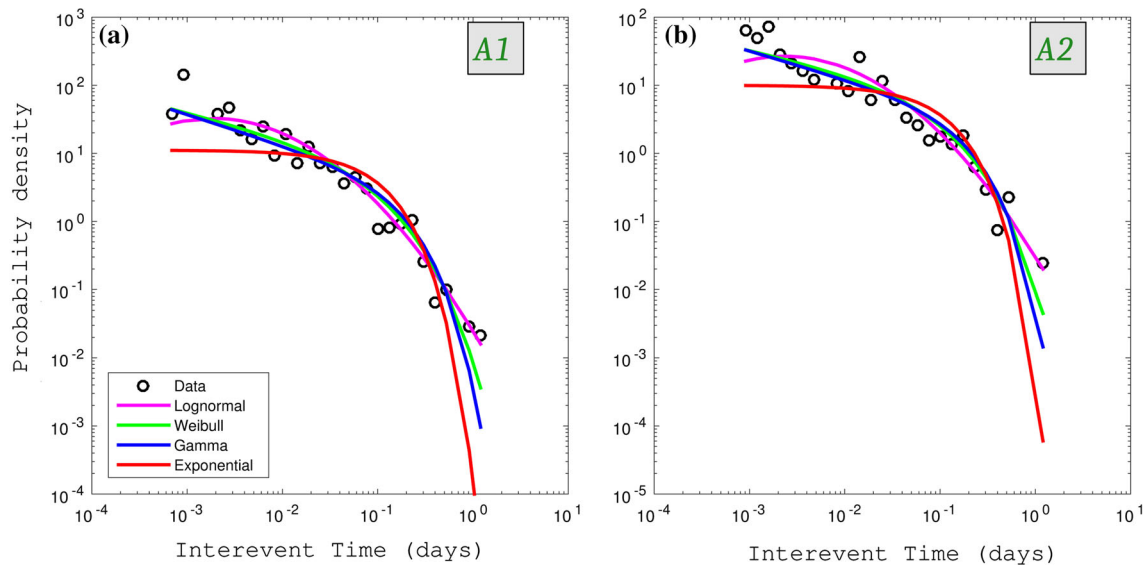
Fig. 11 Probability density function of the interevent times for two sub-periods (A1 and A2) along with the fit of different statistical distributions (lognormal, Weibull, gamma and exponential)
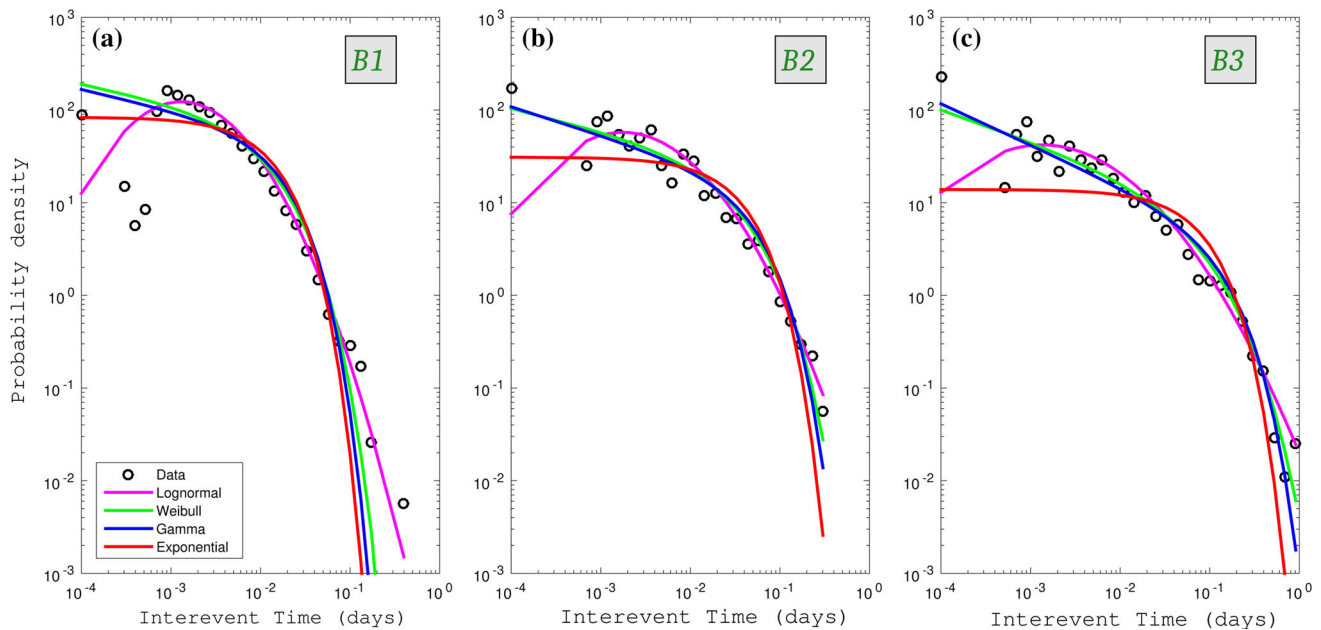
Fig. 12 Same as Fig. 11 for three sub-periods (B1, B2 and B3)

boundary of the swarm-like sequences and mainshock–aftershock one. This indicates a rather complex mechanism which cannot be strictly classified in any of these two types. The ETAS fit revealed that the observed seismicity rate deviates from the modeled transformed time. In cases of a Poisson process, the observed and modeled rate should coincide; otherwise, a different process governs the earthquake occurrence. This observation led to the investigation of the interevent time distribution by fitting several statistical distributions to the empirical one. The exponential is also tested among the selected distributions (lognormal,

Weibull and gamma) in order to test whether a Poisson process is suitable to describe the seismicity occurrence. However, in all cases the interevent times in each sub-period showed that lognormal distribution best fits to the empirical one, implying earthquake triggering.

Seismic swarms like the one investigated in this study have to be taken into account in seismic hazard assessment. Such crises may occur frequently enough as to contribute to the budget of seismic moment release on the associated faults. Their appearance may explain why no strong earthquake has been reported in this area. Given that the

historical catalog is complete for M7 events for the last several centuries and the lack of relevant information for smaller in magnitude events ($M = 5.0$–6.0), this can be attributed to the fact that the accumulated strain is released by swarm-like activity in smaller faults optimally oriented to the N–S back arc extension. This kind of activity might be driven by fluid pore pressure variations which can be better unraveled by taking into account the presence of migrating fluids.

References

Chouliaras G, Kassaras I, Kapetanidis V, Petrou P, Drakatos G (2015) Seismotectonic analysis of the 2013 seismic sequence at the western Corinth Rift. J Geodyn 90:42–57. https://doi.org/10.1016/j.jog.2015.07.001

Corral A (2006) Dependence of earthquake recurrence times and independence of magnitudes on seismicity history. Tectonophysics 424:177–193. https://doi.org/10.1016/j.tecto.2006.03.035

Demir MM, Baba A, Atilla V, Inanli M (2014) Types of the scaling in hyper saline geothermal system in northwest Turkey. Geothermics 50:1–9. https://doi.org/10.1016/j.geothermics.2013.08.003

Duverger C, Godano M, Bernard P, Lyon-Caen H, Lambotte S (2015) The 2003–2004 seismic swarm in the western Corinth rift: evidence for a multiscale pore pressure diffusion process along a permeable fault system. Geophys Res Lett 42:7374–7382. https://doi.org/10.1002/2015GL065298.1

Evison FF (1977) The precursory earthquake swarm. Phys Earth Planet Inter 15:19–23

Evison F, Rhoades D (2000) The precursory earthquake swarm in Greece. Ann Geofis 43:991–1009

Farrell J, Husen S, Smith RB (2009) Earthquake swarm and b-value characterization of the Yellowstone volcano-tectonic system. J Volcanol Geotherm Res 188:260–276. https://doi.org/10.1016/j.jvolgeores.2009.08.008

Fischer T, Horálek J, Hrubcová P, Vavrycuk V, Brauer K, Kampf H (2014) Intra-continental earthquake swarms in West-Bohemia and Vogtland: a review. Tectonophysics 611:1–27. https://doi.org/10.1016/j.tecto.2013.11.001

Hainzl S, Ogata Y (2005) Detecting fluid signals in seismicity data through statistical earthquake modeling. J Geophys Res 110:1–10. https://doi.org/10.1029/2004JB003247

Kapetanidis V, Deschamps A, Papadimitriou P, Matrullo E, Karakonstantis A, Bozionelos G, Kaviris G, Serpetsidaki A, Lyon-Caen H, Voulgaris N, Bernard P, Sokos E, Makropoulos K (2015) The 2013 earthquake swarm in Helike, Greece: seismic activity at the root of old normal faults. Geophys J Int 202:2044–2073. https://doi.org/10.1093/gji/ggv249

Karakostas VG, Papadimitriou EE, Karakaisis GF, Papazachos CB, Scordilis EM, Vargemezis G, Aidona E (2003) The 2001 Skyros, Northern Aegean, Greece, earthquake sequence: off-fault aftershocks, tectonic implications, and seismicity triggering. Geophys Res Lett 30:10–13. https://doi.org/10.1029/2002GL015814

Karakostas VG, Papadimitriou EE, Tranos MD, Papazachos CB (2010) Active seismotectonic structures in the area of Chios island, North Aegean Sea, revealed from microseismicity and fault plane solutions. Bull Geol Soc Greece XLII:2064–2074

Karakostas V, Karagianni E, Paradisopoulou P (2012) Space-time analysis, faulting and triggering of the 2010 earthquake doublet in western Corinth Gulf. Nat Hazards 63:1181–1202

Karakostas V, Papadimitriou E, Gospodinov D (2014) Modelling the 2013 North Aegean (Greece) seismic sequence: geometrical and frictional constraints, and aftershock probabilities. Geophys J Int 197:525–541

Kiratzi A, Sokos E, Ganas A, Tselentis A, Benetatos C, Roumelioti Z, Serpetsidaki A, Andriopoulos G, Galanis O, Petrou P (2008) The April 2007 earthquake swarm near Lake Trichonis and implications for active tectonics in western Greece. Tectonophysics 452:51–65. https://doi.org/10.1016/j.tecto.2008.02.009

Klein FW (2000) User's guide to HYPOINVERSE-2000, a Fortran program to solve earthquake locations and magnitudes, Open File Rep. 02–171, Ver. 1.0, U.S. Geological Survey, Menlo Park, USA

Kyriakopoulos C, Chini M, Bignami C, Stramondo S, Ganas A, Kolligri M, Moschou A (2013) Monthly migration of a tectonic seismic swarm detected by DInSAR: southwest Peloponnese, Greece. Geophys J Int 194:1302–1309. https://doi.org/10.1093/gji/ggt196

Lombardi AM (2015) Estimation of the parameters of ETAS models by simulated annealing. Sci Rep 5:8417. https://doi.org/10.1038/srep08417

Lombardi AM (2017) SEDA: a software package for the statistical earthquake data analysis. Sci Rep 7:44171. https://doi.org/10.1038/srep44171

Mesimeri M, Papadimitriou E, Karakostas V, Tsaklidis G (2013) Earthquake clusters in NW Peloponnese. Bull Geol Soc Greece, XLVII, pp 1167–1176

Mesimeri M, Karakostas V, Papadimitriou E, Schaff D, Tsaklidis G (2016) Spatio-temporal properties and evolution of the 2013 Aigion earthquake swarm (Corinth Gulf, Greece). J Seismol 20:595–614. https://doi.org/10.1007/s10950-015-9546-4

Mesimeri M, Karakostas V, Papadimitriou E, Tsaklidis G, Tsapanos T (2017) Detailed microseismicity study in the area of Florina (Greece): evidence for fluid driven seismicity. Tectonophysics 694:424–435. https://doi.org/10.1016/j.tecto.2016.11.027

Mogi K (1963) Some discussions on Aftershocks, Foreshocks and Earthquake Swarms- the Fracture of a Semi-infinite body caused by an inner stress origin and its relation to the earthquake phenomena. Bull Earthq Res Inst 41:615–658

Ogata Y (1992) Detection of precursory relative quiescence before great earthquakes through a statistical model. J Geophys Res 97:19845. https://doi.org/10.1029/92JB00708

Ogata Y (1998) Space-time point process models for earthquakes occurrences. Ann Inst Stat Math 50:379–402

Pacchiani F, Lyon-Caen H (2010) Geometry and spatio-temporal evolution of the 2001 Agios Ioanis earthquake swarm (Corinth Rift, Greece). Geophys J Int 180:59–72. https://doi.org/10.1111/j.1365-246X.2009.04409.x

Panagiotopoulos DG, Papazachos BC (1985) Travel times of Pn-waves in the Aegean and surrounding area. Geophys J R Astron Soc 80:165–176

Papadimitriou E, Gospodinov D, Karakostas V, Astiopoulos A (2013) Evolution of the vigorous 2006 swarm in Zakynthos (Greece)

and probabilities for strong aftershocks occurrence. J Seismol 17:735–752. https://doi.org/10.1007/s10950-012-9350-3

Schaff DP, Waldhauser F (2005) Waveform cross-correlation-based differential travel-time measurements at the northern California seismic network. Bull Seismol Soc Am 95:2446–2461

Scholz CH (1968) Microfracturing and the inelastic deformation of rock in compression. J Geophys Res 73:1417. https://doi.org/10.1029/JB073i004p01417

Scholz CH (2002) The mechanics of earthquakes and faulting, 2nd edn. Cambridge University Press, Cambridge, p 496

Schorlemmer D, Wiemer S, Wyss M (2005) Variations in earthquake-size distribution across different stress regimes. Nature 437:539–542. https://doi.org/10.1038/nature04094

Shapiro SA (2015) Fluid-induced seismicity. Cambridge University Press, Cambridge, p 298

Shelly DR, Hill DP, Massin F, Farell J, Smith RB, Taira T (2013) A fluid-driven earthquake swarm on the margin of the Yellowstone caldera. J Geophys Res E Planets 118:4872–4886. https://doi.org/10.1002/jgrb.50362

Sornette D, Helmstetter A (2002) Occurrence of finite-time-singularities in epidemic models of rupture, earthquakes and starquakes.

Phys Rev Lett 89:1–4. https://doi.org/10.1103/PhysRevLett.89.158501

Sornette D, Werner MJ (2005) Constraints on the size of the smallest triggering earthquake from the epidemic-type aftershock sequence model, Båth's law, and observed aftershock sequences. J Geophys Res 110:1–11. https://doi.org/10.1029/2004JB003535

Sykes L (1970) Earthquake swarms and sea floor spreading. J Geophys Res 75:6598–6611

Urbancic TI, Trifu CI, Long JM, Young RP (1992) Space-time correlations of b values with stress release. Pure appl Geophys 139:449–462. https://doi.org/10.1007/BF00879946

Waldhauser F, Ellsworth WL (2000) A Double-difference earthquake location algorithm: method and application to the Northern Hayward Fault, California. Bull Seismol Soc Am 90:1353–1368. https://doi.org/10.1785/0120000006

Wessel P, Smith WHF (1998) New, improved version of the generic mapping tools released. EOS Trans Am Geopys Union 79:579

Wiemer S, Wyss M (2000) Minimum magnitude of completeness in earthquake catalogs: examples from Alaska, the Western United States, and Japan. Bull Seismol Soc Am 90:859–869. https://doi.org/10.1785/0119990114